Mon. Not. R. Astron. Soc. **000**, 1–?? (2015) Printed 16 May 2015 (MN LATEX style file v2.2)

# A method to search for large-scale concavities in asteroid shape models

M. Devogèle[1,2], J.P. Rivet[2], P. Tanga[2], P. Bendjoya[2], J. Surdej[1,3], P. Bartczak[4], J. Hanus[2]

[1] *Institut d'Astrophysique et de Géophysique, Allée du 6 Août 17, Sart Tilman, Bât. B5c, 4000 Liège, Belgique*
[2] *Université de Nice Sophia Antipolis, Observatoire de la Côte d'Azur ,CNR UMR 7293 Laboratoire Lagrange, France*
[3] *Directeur de Recherches honoraire du FNRS*
[4] *Astronomical Observatory Institute, Faculty of Physics, Adam Mickiewicz University, Sloneczna 36, 60-286 Poznań, Poland*

**ABSTRACT**

Light curve inversion is proven to produce an unique model solution only under the hypothesis that the asteroid is convex. However, it was suggested that the resulting shape model, for the case of non-convex asteroid, is the convex-hull of the true asteroid non-convex shape. While a convex shape is already useful to provide the overall aspect of the target, much information about real shapes is missed, as we know that asteroids are very irregular. It is a commonly accepted evidence that large flat areas sometimes appearing on shapes derived from light curves correspond to concave areas, but this information has not been further explored and exploited so far. We present in this paper a method that allows to predict the presence of concavities from such flat regions. This method analyzes the distribution of the local normals to the facets composing shape models to predict the presence of abnormally large flat surfaces. In order to test our approach, we consider here its application to a large family of synthetic asteroid shapes, and to real asteroids with large scale concavities, whose detailed shape is known by other kinds of observations (radar and spacecraft encounters). The method that we propose is proven to be reliable and capable of providing a qualitative indication of the relevance of concavities on well-constrained asteroid shapes derived from purely photometric data sets.

**Key words:** minor planets, asteroids, general < Planetary Systems

## 1 INTRODUCTION

Knowledge about the shape of asteroids constitutes an essential piece of information to understand the complex process of asteroid formation and collisional evolution. This is a crucial information not only to measure the properties of individual objects (such as volume and density) but also to characterize the nature of the asteroid population as a whole.

Over the past decades, more and more asteroid shapes have become available. First, the shapes of the biggest asteroids were determined. They appeared to very closely match spheres or ellipsoids. For long, the three-axial ellipsoid model has been the general framework for asteroid shapes determination and, most of the time, only their relative axis ratios could be determined. In 1991, for the first time, a spacecraft (the Galileo probe) performed a close approach to the asteroid (951) Gaspra providing a close look at one of these objects. This first close fly by of an asteroid revealed a detailed shape (Belton et al. 1992) that strongly deviates from the ellipsoid approximation. In 2000, radar ranging has unveiled the "dog's bone shape" of the asteroid (216) Kleopatra (Ostro et al. 2000). Such examples nicely demonstrate the great diversity of asteroids morphologies and the need to develop shape determination methods that can go beyond simple geometric shapes. For this sake, in 2001, Kaasalainen & Torppa (2001); Kaasalainen et al. (2001, hereafter KT and KTM, respectively) presented a light curve inversion technique to obtain approximate shape models for asteroids from a set of dense time series of photometric observations (light curves).

Since then, this method and its variants have been successfully applied to a few hundred objects. However, the solution of this inverse problem is known to be unique only for convex bodies (KT and KTM, 2001). In order to obtain non-convex asteroid shape models, the use of additional constraints – independent from photometry – is needed, such as high-resolution profiles obtained by Adaptive Optics or stellar occultations (Marchis et al. 2006). The inversion algorithm KOALA (Carry et al. 2010; Kaasalainen 2011) is able

to take all these types of observations into account in order to determine reliable non-convex shapes. As now, only a few asteroids have enough data for such techniques to permit a reliable modeling by KOALA.

Still, concavities can be very relevant in a variety of situations. In 2006, Cellino et al. (2006) reported the discovery of the anomalous polarimetric properties of (234) Barbara. The polarization of asteroids is usually studied as a function of the so-called "phase angle", that is the angle subtended by the directions of the observer and the Sun, as seen from the asteroid. Usually, at small phase angle the polarization plane is parallel to the scattering plane on which the phase angle is defined, and is defined by a negative sign. A transition to a perpendicular (positive) polarization occurs at the "inversion" phase angle. In the case of (234) Barbara the negative branch exhibits a stronger polarization and an inversion angle uncommonly large, around 30°. Other asteroids (hereafter called "Barbarians") with similar polarization properties were found later on in 2008, 2009 and 2014 (Gil-Hutton et al. 2008; Masiero & Cellino 2009; Cellino et al. 2014; Gil-Hutton et al. 2014).

As a possible explanation to the peculiar polarimetric behavior of "Barbarian" asteroids, Cellino et al. (2006) suggested that large concavities might play a role by producing a large variety of scattering and incidence angles. Recent observations of (234) Barbara (Tanga et al. 2015) have shown the presence of large concavities through interferometric measurements (Delbo et al. 2009) and well-sampled profiles obtained during two stellar occultations. The observation of concavities on (234) Barbara is of course not sufficient *per se* to prove the link between concavities and anomalous "Barbarian-like" polarization, which remains to be proven on more solid theoretical and observational grounds. In fact, at the same time a link of polarization to the asteroid composition is certainly present, as all Barbarians belong to the spectroscopic L and Ld classes of the SMASS taxonomy (DeMeo et al. 2009), with a few exception of the K types. Their near-infrared spectra exhibit a large absorption feature around $2\mu m$ that has been related to the presence of spinel inclusions from fluffy-type CAIs (Calcium-Aluminium-rich Inclusions) (Sunshine et al. 2007, 2008).The meteorite analog of these asteroids would be similar to CO3/CV3 meteorites, but with a surprisingly high CAIs percentage ($\sim$ 30%) never found among known meteorites. If this hypothesis was true, the Barbarians should have formed in an environment very rich in refractory materials, and would contain the most ancient mineral assemblages of the Solar System.

Disentangling these two possible sources for the anomalous polarization is important, and it would require to combine polarimetric observations to approaches capable of detecting concavities. Such approaches exist, but at present they are not suited to be applied systematically on a representative sample of asteroids. For instance, radar ranging is much more efficient for Near Earth Objects, due to the power decay with distance$^{-4}$ in the signal. Also, sampling a shape by stellar occultations requires a considerable effort in terms of the number of observing stations for a single event, and events that are accurately predictable are rather rare.

We thus think that it is interesting to investigate an approach relying upon large observational data sets that are already existing or easy to obtain. In this paper, we present a new large concavity detection technique which relies on the analysis of the convex shape model determined by light curve inversion, only.

Although light curve inversion methods cannot lead to unambiguous shape determination for non-convex objects, KT (2001) showed that even for highly non-convex objects, the shape model obtained through light curve inversion is very close to the convex-hull of the original surface. The convex-hull of a non-convex shape represents the minimal convex volume which encloses the original shape. Consequently, large concavities are replaced by large flat surfaces.

In section 2, we introduce a new technique for the automatic detection of large flat surfaces. This relies on the definition of a quantitative "local flatness degree" which can be easily computed for a given convex shape model. This leads to a quantitative user-independent estimate of the flatness of a given region at the surface of a model. A first numerical validation of this method is presented in section 3, based upon a population of random synthetic shapes. In section 4, the same kind of validation is described, but using a population of shapes produced by light curve inversion. This incorporates in the validation process, the specificity of shape models obtained by light curve inversion. There exist a few asteroids for which the shape is well know. The method has been applied on their shape model determined by the light curve inversion method (using the real observed light curves) and compared with their real shape. Finally, a discussion and some possible applications of this method are presented in section 5.

## 2 AUTOMATIC FLAT SURFACE DETECTION ON SHAPE MODELS

In this section, a new algorithm to detect flat areas on a shape model is introduced, based on a statistical analysis of the angular distribution of the vectors normal to the shape surface.

A shape model consists of a number of points ("vertices") represented by their Cartesian coordinates $(x, y, z)$. The points are associated by triplets to define triangular facets. All the facets together build up a close polyhedral surface.

The normal directions to all of these facets intersect the surface of a sphere enclosing the analyzed shape, thus defining a set of points on that sphere. The statistical properties of this spherical cloud of points bears the signature of the presence/absence of flat areas. Indeed, if this cloud of points is more or less uniformly distributed on the sphere, then no large flat area is present at the surface of the shape model (upper part of Fig. 1). On the contrary, if it displays some concentrations, then it is likely to be due to the presence of large flat areas (lower part of Fig. 1). In fact, for each of them, local normals will point toward similar directions. Our aim is to derive, from this simple evidence, a quantitative "flatness" criterion.

### 2.1 Subdivision of the sphere

The first step consists in sorting all the normal vectors into "bins" tiling the sphere. This rises the problem of tiling a

sphere into $N_b$ elementary domains, with nearly-equal surfaces. This is not a trivial issue. For simplicity reasons, we chose to restrict ourselves to triangular tiles, and to set the vertices of this triangular tiling according to an algorithmic solution (Saff & Kuijlaars 1997) of the so-called "Fekete problem" (Fekete 1923). Our method consists in spreading a number of points over the surface of a sphere, so as to maximize the sum of the inverse pairwise distances. If all those points were bearing an equal electrical charge, this distribution would minimize the total electrostatic Coulomb energy. Then, the triangular bins are constructed from this cloud of points, through the Delaunay triangulation method (Delaunay 1934). This algorithm does not lead to triangular tiles (bins) with exactly equal areas. The slight discrepancies in triangles areas are compensated by a normalization factor in our procedure. The triangles displayed on both spheres on the right panel of Fig. 1 represent one example of such tilling.

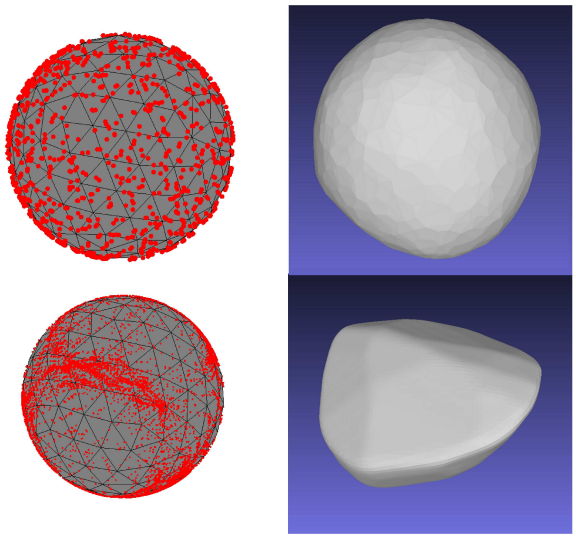

**Figure 1.** Distribution of normal vectors for two morphological cases. Upper part: a convex shape without extended flat surfaces. Lower part: a convex shape with large flat surfaces, obtained as the convex hull of a non-convex shape. The 3D view of the models are displayed on the rightmost panel. The distributions of the normal vectors appear on the leftmost panel. The black triangular meshing represents the bins tiling the sphere. The red dots represent the normal vectors. On the upper part, the body contains almost no flat regions, and thus the normal vector distribution does not exhibit any clearly visible large scale inhomogeneity. On the lower right figure, the body possesses very large flat regions. This leads to a highly inhomogeneous normal vector distribution.

### 2.2 Local flatness degree and detection threshold

The points associated to the normals to the triangular facets are then grouped over the bins on the sphere. A nearly spherical shape would lead to nearly equally populated bins. On the contrary, an irregular shape with large flat surfaces results in a concentration of the normals in a few specific bins (see Fig. 1). Thus, a local "flatness degree" can be estimated from the cumulative area of contiguous facets whose normal vectors fall within a given bin, expressed as a fraction of the total surface. The typical size of the bins (which depends on their number) will determine the largest angle between two normal vectors falling into a single bin. In other words, the size of the bins controls the tolerance of the method on the flatness of the areas to be detected as "large flat areas".

After having computed the "flatness degree" for all the bins, one has to decide whether a given bin, with a given flatness index, is to be considered as representing a flat area or not. This is done by choosing a detection threshold $\Omega$ on the flatness degree.

Of course, this choice can appear as rather arbitrary. In a very general situation of a theoretical shape without any specific limit on the scale of the concavities, $\Omega$ can simply be tuned for choosing the minimal size of flat surfaces that one wants to detect.

However, in practice, the structures present on the asteroid shapes that we analyze are not scale-free. Light curve inversion can't resolve small-scale structures – craters, for example – while it reproduces concavities that are typically larger than 20-25% the diameter of the object. We show in the following that, in such a situation, a suitable value for the threshold $\Omega$ exists, and depends on the number of bins $N_b$ into which the unit sphere is divided. As shown below, this optimal $\Omega$ can be chosen so as to maximize the detection efficiency.

The basic principles of our approach are illustrated in Fig. 2, on a synthetic, simplified 2D shape.

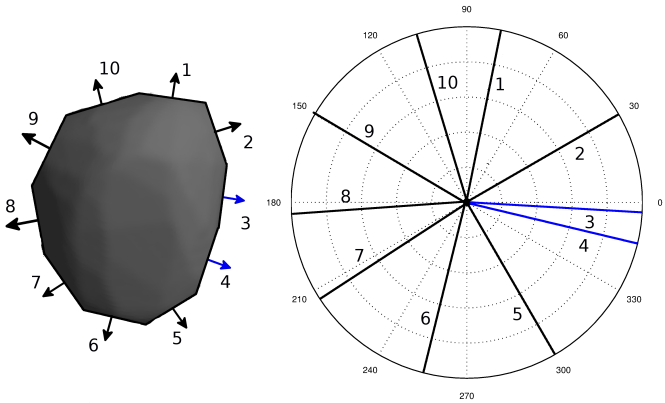


**Figure 2.** Low resolution 2D version of our method, for illustration purpose. The left part of the figure displays a 2D convex shape model divided into 10 segments with lengths nearly equal to the unity. The arrows, labeled from 1 to 10, represent the normal vectors of each segment. The right figure shows a polar diagram, divided into 12 equal angular bins separated by dotted lines, where the normal vectors of the 10 segments are displayed. In this simplified case, most bins contain zero or one normal vector, except one bin, which contains the normal vectors of segments 3 and 4. This bin collects nearly 20% of the total length of the segments, whereas all the other bins collect at most some 10% of the total length. If a threshold of 15% is chosen, the segments 3 and 4 are pointed out as associated with a "large flat zone", possibly revealing a hidden large concavity.

## 3 VALIDATION ON SYNTHETIC SHAPE MODEL

### 3.1 Synthetic shape model population

To assess the role of $N_b$ and $\Omega$ we have implemented a set of tests on a population of randomly generated synthetic (but realistic) asteroid-like shape models. The procedure also provides information on the robustness of our method if non-optimal parameters values are used.

The convex shape models are generated through the following iterative process, starting from an initial regular low-order polyhedron chosen at random. A vertex is added at the geometrical center of each face of the polyhedron. Then, it is shifted along the normal to the facet, in the outward pointing direction, of a positive distance chosen at random. New facets are then built, including the new vertices, by means of a Delaunay triangulation.

If the resulting new polyhedron happens to be non-convex, the last iteration step is canceled and performed again. The number of facets of the resulting shape model is controlled by the number of iterations of this process. The general morphology of the shape model can be controlled by the statistics of the outward random shifts, at each iteration of the process: shift distributions which are sharply centered on very small values, compared to the initial polyhedron's size, will lead to a final shape very close to the initial polyhedron. Conversely, distributions centered on larger values, identical for all iterations will produce nearly spherical shapes. Irregular convex shapes can be produced by choosing, at each iteration, a distribution peaked on smaller and smaller values. Finally, the aspect ratios $b/a$ and $c/b$ of the best fitted ellipsoid are computed. They provide the global flattening and elongation of the shape, that can be adjusted by applying an affine map. An example of such a generated convex shape model is shown in the left panel of Fig. 3.

A statistical set of 300 random synthetic convex shapes with no significant flat areas has been generated this way. To simulate a realistic asteroid population, the axis ratios $b/a$ and $c/b$ have been generated as explained above, in the range from 1 to 0.6 and from 1 to 0.8, respectively.

A statistical set of 300 non-convex shape models has also been generated. This set has been generated using Gaussian spheres (Muinonen 1998). Each sample has been obtained by deforming an initial sphere with a random combination of spherical harmonics, up to the azimuthal degree 8. The random coefficients of this combination have been chosen according to centered normal laws with a standard deviation rapidly decreasing as the azimuthal order increases. An example of such a generated non-convex shape model is also shown in Fig. 3. Finally, the convex hulls of all these non-convex shape models have been computed, yielding a population of 300 convex shapes presenting some flat areas.

Incidentally, we show in Fig. 4 the histogram of the maximal amplitude (*i*.e with an aspect angle equal to 90°) of light curves generated from our whole shape population (by the method described in sect. 4.1). When compared to the same distribution for real objects, we can see that the range of the represented value is not very different, with a slightly less populated distribution for low and high amplitude values.

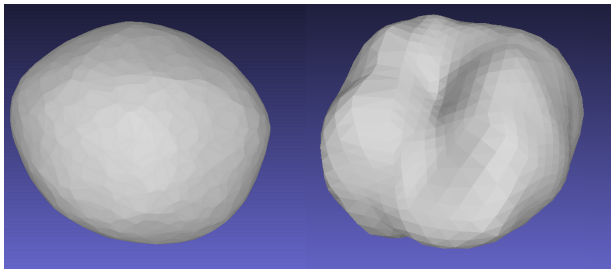

**Figure 3.** Example of a 3D view of a randomly generated shape model. Left panel: convex shape model. Right panel: non-convex shape model.

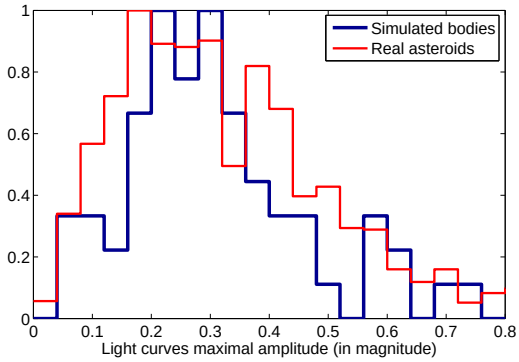


**Figure 4.** Histograms of the maximal amplitude of the light curves simulated using the synthetic shape models (in blue) and for real asteroids light curves (in red).

### 3.2 Threshold value ($\Omega$) and bin sizes: detection efficiency

The value of $\Omega$ is a key issue for the efficiency and selectivity of this method. In order to determine the optimal value of this threshold for a different number of subdivision bins of the unit-sphere $N_b$, we have performed a numerical test on the synthetic convex and non-convex shape populations. These two populations have been used as a test bench to estimate the detection efficiency of our criterion, and to adjust the threshold $\Omega_m$ so as to maximize this detection efficiency. All these shape models have a number of facets ranging between 1700 and 2050, in order to be as close as possible to the typical number of facets of shape models produced by real light curve inversion.

We define the detection efficiency as the percentage of the sample in the aforementioned set of synthetic shapes, which leads to a correct detection. In order to define a correct detection, some assumptions need to be done. First, no flat surface is present on the generated convex shape models. Secondly, there is at least one flat surface present on the convex-hull of the generated non-convex shape models. Using these assumptions, we can define a good detection as: no flat surface detected in the first population (convex), and detection of at least one flat surface in the second population (convex-hull of the non-convex shape models). The detection efficiency has been computed over this $300 + 300$ shape models population for various values of the detection

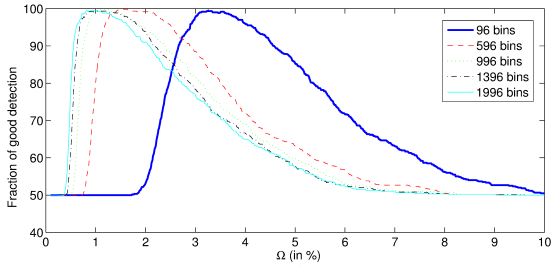


**Figure 5.** Detection efficiency for Ω varying from 0.1 to 10% when using the model with a number of 96 (continuous thick blue line), 596 (dashed red line), 996 (point green line), 1396 (black line) and 1996 (continuous cyan line), bins, respectively .

.

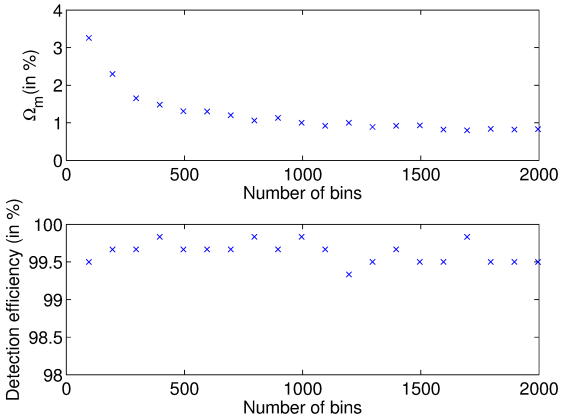


**Figure 6.** Upper graph: The optimal detection threshold $\Omega_m$ as a function of the number of bins. Lower graph: the optimal detection efficiency as a function of the number of bins.

.

threshold Ω and for a number of bins varying from 96 to 1996.

The results of these simulations (Figs. 5 and 6) show that the efficiency of the method (always higher than 99% of good detection for a threshold equal to $\Omega_m$) is nearly independent on the number of bins, at least over a wide range of values. On the contrary, $\Omega_m$ clearly depends on the number of bins. For a number of bins equal to 96, $\Omega_m$ is equal to 3.26% of the total surface area, but when the number of bins is equal to 1996, $\Omega_m$ is reduced to 0.83%. As seen in Fig. 6, the optimal threshold $\Omega_m$ increases when the number of bins decreases. Figure 5 shows the detection efficiency for Ω varying from 0.1% to 10% for different numbers of bins.

These results imply that the number of bins does not impact significantly the detection efficiency, but determines the optimal threshold value to be used.

A final test is to check if, for a real asteroid shape, the detected flat surfaces correspond to the position of the concavities.

A low-resolution shape model of the asteroid (433) Eros obtained by the NEAR probe (Gaskell 2008), has been used to perform this test. First, a convex-hull has been computed for this non-convex shape. Then, our flat area detection algorithm has been applied.

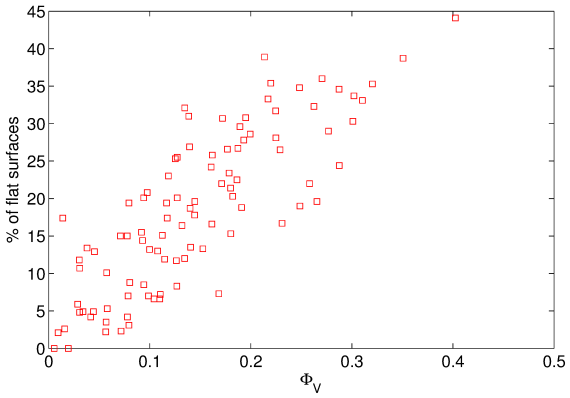


**Figure 8.** Relation between the fraction of flat surfaces detected over the convex-hull of a non-convex shape model and the volume ratio ($\Phi_V$) of the same model.

Fig. 7 displays the results of this numerical experiment. (433) Eros has a highly non-convex shape and this non-convexity is not only due to small or medium-sized craters. Those concavities, which appear as large flat areas on the convex-hull have been successfully detected by our algorithm (red triangular facets visible on the rightmost image of Fig. 7). The number of bins used for this computation was 96 and the detection threshold Ω was 3.26% which corresponds to the optimal threshold value.

### 3.3 Correlation between the fraction of flat surfaces and the presence of concavities

Until now, only binary tests have been conducted: large flat areas are present or not. In this section, the fraction of flat surfaces detected on the shape model will be analyzed. This fraction of flat surfaces is the ratio between the cumulative area of all flat surfaces detected and the total area of the shape model.

An important issue of the detection method is to check if the fraction of detected flat surfaces over the convex shape model (we call this parameter $\eta_S$) can be correlated with the "degree of non-convexity" of the non-convex shape model. There is no unique and optimal parameter to express at which point a shape model is non-convex. We choose a parameter which corresponds to the fraction of the convex-hull volume occupied by the concavities ($\Phi_V$). This fraction can be determined by computing the volume enclosed by the convex-hull ($V_{CH}$) and the volume enclosed by the original shape model ($V_S$). Then, $\Phi_V = \frac{V_{CH}-V_S}{V_{CH}}$. For a perfectly convex body, the volume occupied by the concavities is null and then $\Phi_V$ is equal to zero. If concavities are present, $\Phi_V$ is greater than zero, but always less than 1. We present in Fig. 8 the fraction of flat surfaces detected over the convex-hull of non-convex synthetic shape models as a function of the fractional volume of the concavities. A correlation between these two parameters is clearly visible.

One should note that in principle the volume of a concavity can vary independently from the surface of the flat area enclosing it on the convex hull. Again, we stress here that the typical morphology of the analyzed shapes exhibits smooth and large concavities, typically. Under this hypoth-

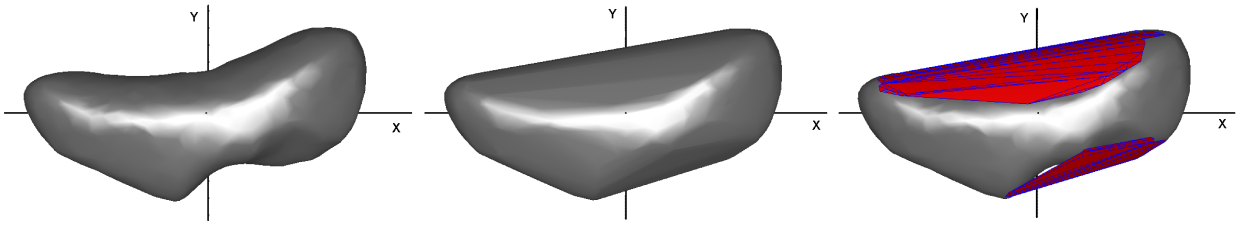


**Figure 7.** Application of the flat areas detection method to the convex-hull of the shape model of the asteroid (433) Eros. The leftmost image represents a low-resolution (non-convex) shape model of (433) Eros obtained by the NEAR probe; the middle image represents its convex-hull and the rightmost image represents the shape model with the flat areas detected by our method superimposed on it (red facets with blue edges).

esis the existence of a trend such as illustrated in Fig. 8 can be justified. The spread of the points is a direct consequence of the looseness of the relation between $\eta_S$ and $\Phi_V$. For this reason, we should not take our $\eta_S$ values as a quantitative equivalent to concavity. Nevertheless, we can assume that it is a good indicator of the qualitative importance of concavities on the shape of a given body and can be used to compare asteroids which each other.

## 4 VALIDATION ON LIGHT CURVE INVERSION SHAPE MODEL

It was shown in the last section that the detection method is able to differentiate shape models resulting from a convex-hull of a non-convex body and naturally convex shapes. If the light curve inversion process produces models very close to the convex-hull of the non-convex asteroid, we should then be able evaluate the relevance of such non-convexities. As a consequence, it appears that a further validation level, simulating the whole chain from photometry to shape determination and analysis is due.

### 4.1 Photometric simulation procedure

The models generated in the last section have been used to produce synthetic light curves mimicking realistic asteroid observations. To produce the light curves, the spin axis of each shape model has been chosen to be parallel to the principal axis of inertia $J_{\max}$ and pointing in the same direction. The pole coordinates on the sky and its rotational period were chosen randomly in the "Lightcurve Derived Data" (Harris et al. 2014) list of spin axis orientations and rotational periods. In order to mimic the epochs of asteroid observations, we decided to use the time sequence of a real case. The light curves were simulated as if it was the asteroid (236) Honoria that was modelled, based on the data of Lagerkvist et al. (1987); Harris & young (1989) and of other lightcurves that have been obtained[1]. As a consequence the epochs at which observations were obtained for this asteroid were chosen, and the relative positions of the Earth, the Sun and (236) Honoria at these same epochs have also been respected. In this particular case, 49 light curves obtained during 5 different oppositions spread over 34 years time span are available. This choice may seem arbitrary, but it is representative of the series of epochs available for the majority of asteroids for which light curve inversion has been achieved.

The scattered light flux received from the asteroid is computed by a ray-tracing procedure which takes into account concavities and shadowing effects. Uniform albedo is assumed and a commonly adopted combination of the Lambert and Lommel-Seeliger diffusion law (Kaasalainen et al. 2002) is used to model the light scattering process.

### 4.2 Synthetic shape model population: Results and detection efficiency

Using the procedure presented in the last section, a set of 200 convex shape models and a set of 200 non-convex shape has been used to generated, for each of them, synthetic light curves. Each set was processed by the Kaasalainen inversion code (KT and KTM, 2001). The resulting shape model was analyzed by our method.

These sets of shape models have been used to test the detection efficiency after performing the light curve inversion. We have presented in Fig. 9 the results of this test. We see that the results are similar to those obtained when using the convex-hull of the non-convex shape models, implying that light curve inversion does not introduce appreciable effects on the efficiency of concavity detection.

#### *4.2.1 Relation between the percentages of flat surfaces and the volume ratio*

We have also tested if the light curve inversion process keeps the correlation between the fraction of flat surface detection and the volume ratio. The result of light curve inversion process is sensitive to ecliptic pole orientation. As a matter of fact, an asteroid for which the pole is oriented perpendicularly *w*.r.t the ecliptic plane will always be seen "equator on". This leads to a loosely constrained $c/a$ axis ratio. The poles of the shape model will then also be poorly constrained. In order to remove this dependency, 140 sets of spin parameters (chosen in the "Lightcurve Derived Data", Harris et al. (2014)) were used for 100 different synthetic non-convex shape models. For each set of spin parameters, the full process of light curve simulation and light curve inversion was repeated (as explained in the first paragraph of this section). For all the tests hereinafter, the optimal value of $\Omega$ determined above was used.

Fig. 10 shows the fraction of flat surfaces ($\eta_S$) detected

[1] the results of the photometric campaign will be the subject of a forthcoming paper, in prepration

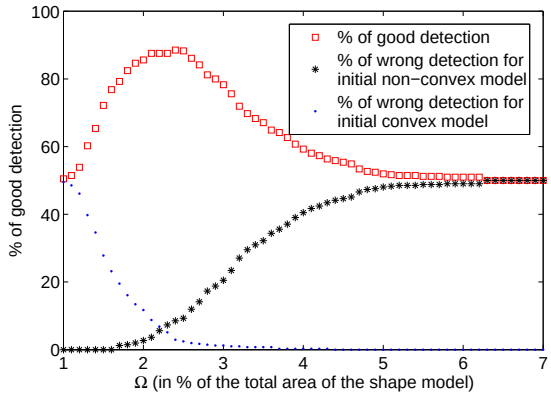


**Figure 9.** Graph showing the fraction of models which are successfully detected as convex or non-convex using shape models which result from the application of the light curve inversion technique (red squares). The fraction of convex models which are detected as non-convex is represented by the blue dots. Finally the black stars represent the non-convex models detected as convex. These curves are plotted as a function of the detection threshold Ω expressed in percent of the total area of the shape model. The method was applied using a number of bins equal to 320. The curves show that for $\Omega = 2.4\%$, we have an optimal successful detection rate equal to 88%.

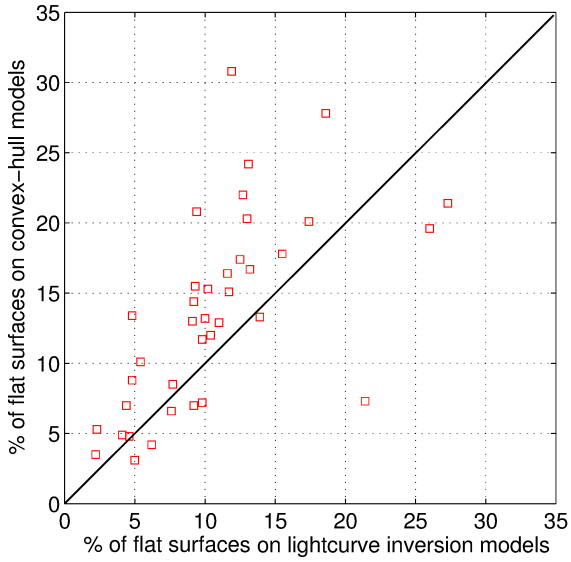


**Figure 11.** Figure showing the fraction of flat surface detected over the convex-hull of a non-convex body and the convex shape resulting from the light curve inversion of these same non-convex models. We can see that there is a clear correlation with a detected fraction slightly smaller for the case of models resulting from light curve inversion.

over the modeled convex shape using the synthetic light curves as a function of the volume ratio of the modeled asteroids. Each black dot represents the average value obtained from the average of the 140 sets of spin parameters adopted for a single object. The corresponding dispersion has also been computed (yielding 1-sigma values from 2 to 4%), but for the sake of plot readability it is not plotted. This figure clearly shows that a correlation between these two parameters exists and that, as expected, the quantity of detected flat surfaces over the inverted shape model increases with the amount of concavity present on the parent body. This dependency is materialized in Fig. 10 by the fit of a power law $\eta_S = a(\Phi_V)^b$ ($a = 54 \pm 8$ and $b = 0.74 \pm 0.08$). This profile (power law) has the interesting property of being monotonic.

Fig. 10 confirms that the fraction of flat surfaces is not strongly constrained in quantitative terms, but it allows to distinguish rather well regular shapes, with a small degree of concavities, from highly irregular ones. The differences between Figs. 10 and 8 can be explained by the fact that light curve inversion does not produce exactly the convex-hull of the shape. Fig. 11 plots the fraction of flat surfaces detected on the convex-hull and on the shape model inverted by light curve inversion. If these models were identical, all points in Fig. 11 would fall along the $x = y$ line. Despite the presence of a clear trend, it can be seen that this is not exactly the case in our simulations. A slightly smaller fraction of flat surfaces is detected on the shape model derived from light curve inversion, than on the convex-hull of the original body.

This result suggests that the model produced by the Kassalainen inversion code is close to the convex-hull, but not identical. The inversion code tends to smooth the flat surfaces which should be present if the model were exactly identical to the convex-hull.

To verify whether the correlation found from our simulated light curve inversion holds true for the case of real asteroids, we plot on the same figure the results related to two other data sets. The first one is a set of asteroids for which the non-convex shapes were modeled by exploiting both light curves and radar ranging and/or stellar occultations information. For them, direct information on the concavities are thus included.

The second set contains asteroid for which the non-convex shape is known with extreme precision (or at least a large fraction of it) thanks to precise reconstructions from radar ranging and/or space probe observations (the points of these two datasets are not fitted). The second set of very precise shape models contains the asteroids (2) Pallas (Durech et al. 2010), (21) Lutetia (Farnham 2013), (216) Kleopatra (Mitchell et al. 1995), (243) Ida (Thomas et al. 1996), (433) Eros (Gaskell 2008) and (951) Gaspra (Thomas et al. 1994).

For both these data sets we computed the concavity volume ratio. In addition, we also compute light curve inversion for those objects having enough photometric data (Durech et al. 2010). The derived convex surfaces were used to compute their fraction of flat surfaces. The results obtained for these asteroids are summarized in Table 4.2.1.

As expected, the value of $\eta_S$ determined for (2) Pallas is very close to zero. This result tends to prove that our model behaves correctly when dealing with a perfect convex body. All these asteroids fall well within the $1\sigma$ confidence level of the fit, represented by the area enclosed by the blue dashed lines.

The final test for our method is devoted to verify that the locations of the concavities that we can identify by light curve inversion correspond in position to the real concavities. To be as close as possible to a real case, we have performed a second numerical experiment on (433) Eros,

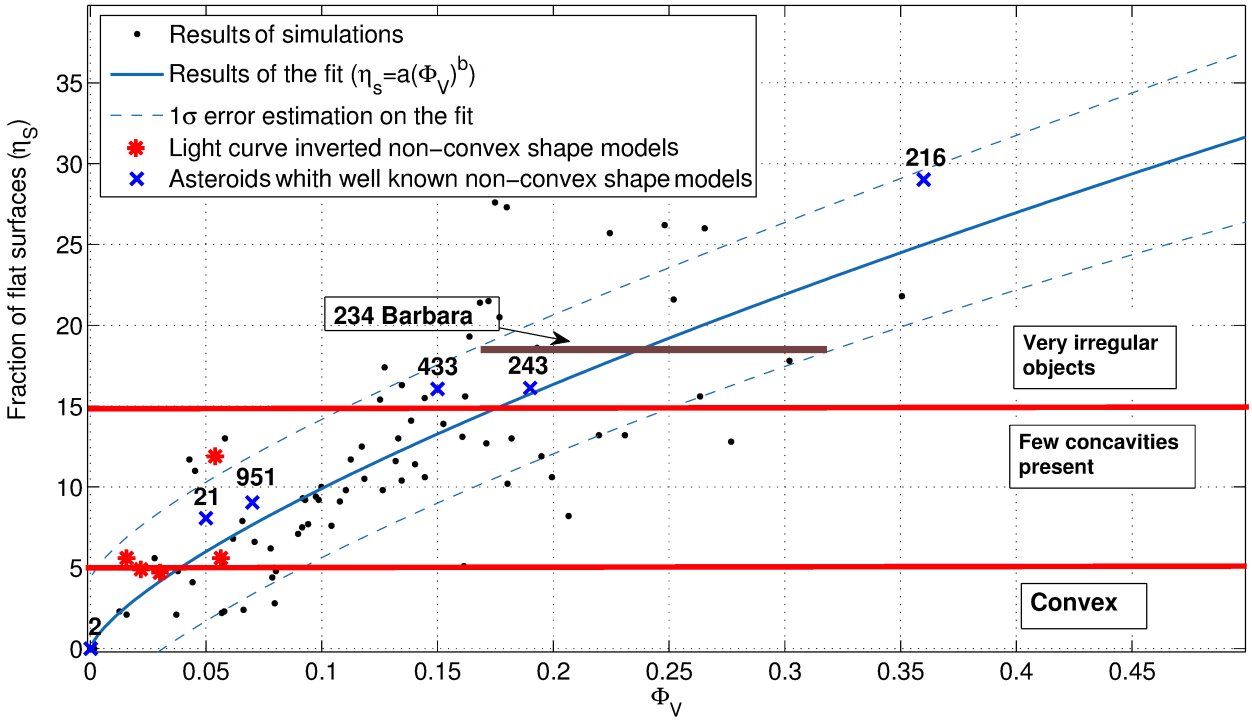


**Figure 10.** Plot of the fraction of flat surfaces detected on simulated shapes against the volume ratio of the parent body. We see that the fraction of flat surfaces detected by our method does well correlate with the volume ratio. We have overplotted to the fit results the expected position of the asteroid (234) Barbara as a function of the fraction of flat surfaces found. We also show the results (red stars) of the method for asteroids for which the KOALA light curve inversion methods produces non-convex shape models (not well constrained). Eventually, with blue crosses, we plot the position of asteroids for which the non-convex shape is very well constrained by space probe observations or other observing techniques such as radar ranging.

| Asteroid | $\Phi_V$ | $\eta_S$ |
|---|---|---|
| (2) Pallas | 0.01 | 0 |
| (21) Lutetia | 0.05 | 8.1 |
| (216) Kleopatra | 0.36 | 29.0 |
| (243) Ida | 0.19 | 16.1 |
| (433) Eros | 0.15 | 16.1 |
| (951) Gaspra | 0.07 | 9.0 |

**Table 1.** Summary of the volume ratio (2nd column) and the fraction of flat surfaces (3rd column) derived for known asteroids (1st column) previously observed with space probes.

similar to the one described in Sec. 3.2. In this case however, the convex-hull has been replaced by the shape model obtained by light curve inversion. This shape model was obtained using the Kaasalainen light curve inversion technique on a set of 134 light curves (Beyer 1953; Dunlap 1976; Millis et al. 1976; Tedesco 1976; Scaltriti & Zappala 1976; Miner & Young 1976; Cristescu 1976; Delaunay 1934; Pop & Chis 1976; Harris et al. 1992; Harris & young 1999; Harris et al. 1995; Krugly & Shevchenko 1994). The result is shown in Fig. 12. Although the convex shape model obtained by light curve inversion is not strictly identical to the convex-hull for this asteroid. Nevertheless, the concavity footprints and positions are almost exactly reproduced, proving that a reasonable guess of the position and extension of large concavities can be correctly obtained.

## 5 CONCLUSION

A new method to infer the presence of concavities on an asteroid from light curve inversion has been presented. Since it has been suggested that flat surfaces are connected with concavities (KT, 2001), for the first time we attempt to exploit this information and to test the solidity of this concept.

Our method detects the presence of large flat surfaces on the convex shape model by analyzing how the normal vectors of the shape model are spread over the unit sphere.

The detection efficiency of concavities, when using the optimal detection threshold $\Omega_m$, can be as high as 99% on the convex hull of synthetic shapes. In the case of light curve inversion, this optimal detection remains around 88%.

Eventually, the detection method provides an estimate of the "convexity degree" of the original shape that can be used as a qualitative information about the complexity of the asteroid shape.

A nice feature of our approach is that it appears to be rather conservative, *i.*e. concavities are slightly under-detected. This avoids spurious concavity identifications. As the photometric data do not bring a relevant signature of the details on the asteroid surface, our concavity detection is not sensitive to those small scale concavities (craters).

This flat detection method was applied to well known non-convex asteroid shapes. The results show that more an asteroid is irregular (with more and more concavities) greater is the fraction of flat surfaces detected by the

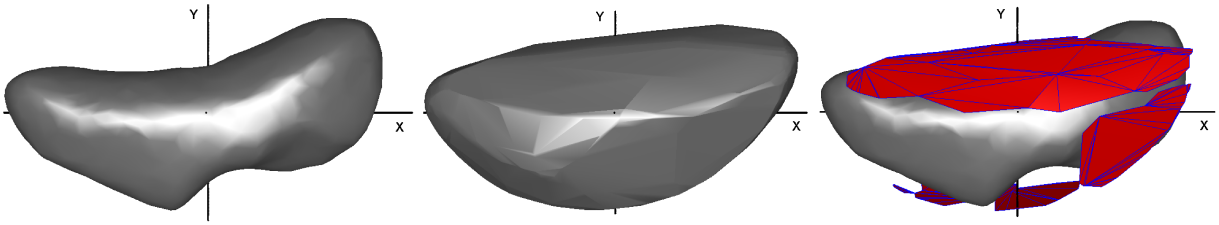


**Figure 12.** Application of the flat area detection method to the shape model obtained by light curve inversion technique of the asteroid (433) Eros. The leftmost image represents a low-resolution (non-convex) shape model of (433) Eros obtained by the NEAR probe; the middle image represents its light curve inversion shape model and the rightmost image represents the shape model with the flat areas detected by our method superimposed on it (red facets with blue edges).

method, consistently with the results obtained on a larger sample of synthetic shapes.

In a forthcoming paper, we plan to apply this detection method to all asteroid shape models currently available, that are well constrained by a sufficient number of light curves. We also plan to apply our method to all asteroids in the category of (234) Barbara, for which light curve inversion models are available, to investigate the possible relation between concavities and anomalous polarimetric response.

## REFERENCES

Belton M.J.S. et al., 1992, Science, 257, 1647
Beyer M., 1953, A.N., 281, 121
Carry B. et al., 2010, Icarus, 205, 460
Cellino A., Bagnulo S., Tanga P., Novakivoc B., Delbo M., 2014, MNRAS, 439, 75
Cellino A., Belskaya I. N., Bendjoya Ph., di Martino M., Gil-Hutton R., Muinonen K., Tedesco E. F., 2006, Icarus, 180, 565
Cristescu C., 1976, Icarus, 39, 42
Delaunay B., Otdelenie Matematicheskikh i Estestvennykh Nauk, 1934, 7 ,793
Delbo M., Ligori S., Matter A., Cellino A., Berthier J., 2009, The A.J., 694, 1228
DeMeo F., Binzel R., Slivan S., Bus S., 2009, Icarus, 160, 180
Dunlap J. L., 1976, Icarus, 28, 69
Durech, J., Vidorin V., Kaasalainen M. 2010, A&A, 512, A46
Farnham, T.L., 2013, SHAPE MODEL OF ASTEROID 21 LUTETIA, RO-A-OSINAC/OSIWAC-5-LUTETIA-SHAPE-V1.0, NASA Planetary Data System
Fekete M., Math. Zeit., 1923, 17, 228
Gaskell, R.W., 2008, Gaskell Eros Shape Model V1.0. NEAR-A-MSI-5-EROSSHAPE-V1.0. NASA Planetary Data System
Gil-Hutton R., Cellino A., Bendjoya Ph., A&A, 2014, 569, A122
Gil-Hutton R., Mesa V., Cellino A., Bendjoya P., Pealoza L., Lovos F., 2008, A&A, 482, 309
Hanus J. et al, 2013, A&A, 551, 16
Harris A.W., Young J.W, 1989, Icarus, 81, 314
Harris A.W., Young J.W., Dockweiler T., Gibson J., Poutanen M., Bowell E. , 1992, Icarus, 95, 115
Harris A.W., Young. J.W., Poutanen M., Bowell E., Tholen D.J., Nicholson P.D., 1995, LPSC, 27, 553
Harris A.W., Young J.W, 1999, Icarus, 81, 314
Harris A.W., Warner B.D., Pravec P., Asteroid Lightcurve Derived Data V14.0., EAR-A-5-DDR-DERIVED-LIGHTCURVE-V14.0. NASA Planetary Data System, 2014
Kaasalainen M., 2011, IPI, 5, 37
Kaasalainen M., Torppa J., Piironen J., 2002, Icarus, 159, 369
Kaasalainen M., Torppa J., 2001, Icarus, 153, 24
Kaasalainen M., Torppa J. and Muinonen K., 2001, Icarus, 153, 37
Krugly Y.N and Shevchenko V.G, 1994, Small Bodies in the Solar System and Their Interaction with the Planets, 113
Lagerkvist C.I., Hahn G., Magnussn P., Rickman H., 1987, A&A Suppl. Ser., 70, 21
Marchis F., Kaasalainen M, Hom E. F. Y, Berthier J., Enriquez J., Herstroffer D., Le Mignant D., de Pater I., Icarus, 2006, 185, 39
Masiero J. and Cellino A., 2009, Icarus, 199, 333
Millis R. L., Bowell E., Thompson D.T., 1976, Icarus, 28, 53
Miner E., Young J., 1976, Icarus, 28, 43
Mitchell D.,Ostro S., Rosema K., Hudson R., Campbell D., Chandler J., Shapiro I., 1995, Icarus, 118, 105
Muinonen K., A&A, 1998, 332, 1087
Ostro. S. et al, Science, 2000, 288, 836
Pop V., Chis D., 1976, Icarus, 28, 37
Saff E.B., Kuijlaars B.J., 1997 The Math. Intelligencer, 1, 5
Scaltriti F., Zappala V., 1976, Icarus, 28, 29
Sunshine J., Connolly H., McCoy T., Bus S., La Croix L., 2007, Lunar and Planetary Institute Science Conference Abstract, 1613
Sunshine J., Connolly H., McCoy T., Bus S., La Croix L., 2008, Science, 320, 514
Tanga P. et al., 2015, MNRAS, 448, 3382
Tedesco E. F., 1976, Icarus 28, 21
Thomas P., Veverka J., Simonelli D., Helfenstein P., Carcich B., Belton M., Davies M., Chapman C., 1994, Icarus 107, 25
Thomas P., Belton M., Carcich B., Chapman C., Davies M., Sullivan R., Veverka J., 1996, Icarus 120, 20